Thermocapillary motion of a solid cylinder near a liquid-gas interface

A. Arslanova,[1] G. Natale,[2] N. Reddy,[3,4] C. Clasen,[1] and J. Fransaer[5]

[1)]*Department of Chemical Engineering, KU Leuven, 3001 Leuven, Belgium*

[2)]*Department of Chemical and Petroleum Engineering, University of Calgary, Calgary, Alberta T2N1N4, Canada*

[3)]*Faculty of Engineering Technology, University of Hasselt, Martelarenlaan 42, 3500 Hasselt, Belgium*

[4)]*IMO-IMOMEC, Wetenschapspark 1, 3590 Diepenbeek, Belgium*

[5)]*Department of Materials Engineering, KU Leuven, 3001 Leuven, Belgium*

(Dated: 8 November 2021)

The motion of a solid, infinitely long cylinder perpendicular to a convective liquid-gas interface due to thermocapillarity is investigated via an analytical model. If the cylinder temperature differs from the bulk temperature, a temperature gradient exist along the liquid-gas interface. This results in surface tension gradients at the liquid-gas interface, causing fluid flow around the particle which induces propulsion. For small particles, and thus small Péclet and Reynolds numbers the steady-state equations for temperature and flow fields are solved exactly using two-dimensional bipolar cylindrical coordinates. The velocity of the cylinder as a function of separation distance from the liquid-gas interface is determined for the case of a constant temperature or a constant heat flux on the surface of the cylinder. A larger temperature gradient at the liquid-gas interface in the latter system leads to a larger cylinder velocity and a higher propulsion efficiency. The thermocapillary effect result in larger force on a cylinder than forces arising from other self-propulsion mechanisms.

I. INTRODUCTION

In recent years, there is a growing interest in the self-propulsion of micron-sized particles[1–3]. The ability of particles to generate field gradients in a surrounding medium, resulting in directed motion, makes them promising candidates for sensing operations[4], moving cargo[5–7] or transporting active pharmaceutical ingredients in the human body[8,9]. The most commonly studied self-propelling particle is a Janus particle with different catalytic properties on opposite sides[10–12]. These particles are able to convert the chemical energy of a fuel into mechanical energy by employing different mechanisms, such as self-electrophoresis[13–15], self-diffusiophoresis[16–18], or bubble propulsion[19,20]. However, the limitation of their self-propulsion linked to the fuel content enforced the search for propulsion mechanisms beyond chemical reactions. For instance, self-propulsion can be also induced by external rotating magnetic field[21], ultrasound[22] or temperature gradients emerging from an asymmetric heating of the particle[23,24]. Additionally, particles are shown to self-propel by local demixing of critical binary[25,26] or non-Newtonian polymer[27] mixtures. Propelling particles by surface tension gradients is another attractive approach at the micron-scale, where surface forces can play a crucial role when the surface-to-volume ratio becomes large. One possible way to establish surface tension gradients is to exploit the temperature dependence of surface tension. An inhomogeneous temperature distribution on the interface between two immiscible liquids, or between a liquid and a gas, leads to gradients in surface tension along the interface. As a result, the liquid will start to move from the region of low surface tension to the region of high surface tension, known as the thermocapillary or Marangoni thermal effect. Marangoni stresses can also originate from an inhomogenous distribution of surface active species at the liquid-gas or liquid-liquid interface. Examples of propulsion by Marangoni flow can be found in nature: for instance, some insects propel along the water surface by the release of surface-active compounds[28].

The motion induced by Marangoni thermal and solutal effects has been extensively investigated for bubbles and drops[29,30]. The spontaneous motion of isotropic drops due to Marangoni flows was addressed analytically[31], as well as experimentally[32]. Marangoni driven motion was also studied for a number of self-propelling systems, such as camphor boats[33,34] and liquid marbles filled with ethanol, which evaporates and subsequently condenses on the water surface resulting in a surface tension gradient, which induces propulsion[35]. Theoretical models were developed for the thermocapillary motion of a disk[36], a spherical particle[37], and an ellipsoid[38] at a liquid-gas interface.

A successful attempt to use the thermocapillary effect to propel a micron-sized gear heated with light was made by Maggi *et al.*[39]. The gear was coated with a light-absorbing layer of carbon and was placed at the water-air interface. They demonstrated that temperature differences even in the millikelvin range can generate large torques due to the thermocapillary effect. The estimated torques are around 1000 pN/μm for every degree of temperature difference, showing the relevance of this approach for the propulsion of micro-particles.

A similar phenomenon emerges when a solid particle is located not at the liquid-gas interface but in the bulk near the interface. That allows us to exploit the propulsion of the particle towards and away from the interface, which, for instance, can be useful in regulating the adsorption of particles to an interface[40]. An analytical model for a sphere moving perpendicular to a liquid-gas interface was developed by Leshansky *et al.*,[41] for a particle near an insulating liquid-gas interface with a constant temperature at the particle surface or a heat source at the particle centre. A formally similar model was treated by Domínguez *et al.*[40,42] for catalytically active or locally heated spherical particles located near a fluid-fluid interface. They noted a generally larger force induced by thermocapillary effect, in comparison to the self-phoretic mechanisms reported in literature, which makes the thermocapillary mechanism interesting as a driving force for self-propelled particles. However, geometries other than spheres need to be considered for a range of applications. For instance, sideways propelled cylindrical particles have a larger effective surface area compared to spherical particles, which is beneficial for sensing or micro-transport. Such anisotropic particles can be produced and are known to self-propel by non-uniform chemical decomposition of hydrogen peroxide[43–45].

The main objective of this work is therefore to derive an analytical solution for the thermocapillary motion of a cylindrical particle moving perpendicular to a convective liquid-gas interface.

II. MODEL

A cylinder with radius a in a liquid at distance d from the liquid-gas interface is shown in Fig. 1. When the temperature of the cylinder differs from the bulk, an inhomogeneous temperature distribution at the liquid-gas interface produces surface tension gradients, giving rise to a thermocapillary flow which sets the cylinder in motion. We assume no contribution to the cylinder velocity by the thermophoretic motion, which can arise due to the temperature difference along the cylinder surface. We calculate the velocity and force acting on the cylinder moving perpen-

dicular to the flat non-deforming liquid-gas interface, assuming that the fluid is Newtonian and incompressible, and that the surface tension depends linearly on temperature[41]:

$$\gamma = \gamma_0 + \frac{\partial \gamma}{\partial T}\left(T - T_\infty\right), \tag{1}$$

where γ is the surface tension $\left[\mathrm{N\ m^{-1}}\right]$, γ_0 is the characteristic value of the surface tension at the reference temperature $T = T_\infty$ $\left[\mathrm{N\ m^{-1}}\right]$, and T is the temperature [K]. The first-order Taylor expansion of the surface tension as a function of temperature in eq. 1 is valid over the moderate temperature ranges investigated in this work, with a temperature coefficient $K_\gamma = -\dfrac{\partial \gamma}{\partial T}$ around 10^{-4} N m^{-1} K^{-1} for most liquids[46]. The surface tension of pure liquids always decreases with temperature, and becomes zero at the supercritical point, thus $\dfrac{\partial \gamma}{\partial T} < 0$. In our analysis, water was chosen as a model liquid, which has a temperature coefficient $K_\gamma = 1.49\ 10^{-4}$ N m^{-1} K^{-1} at $T_\infty = 20\ ^\circ$C[47]. Other physical parameters of the liquid such as viscosity, density and thermal conductivity, are assumed to be constant. The liquid-gas interface is assumed to remain flat. For water-air interface this is a valid assumption due to the high surface tension, which keeps the interface flat, so that the capillary number $\mathrm{Ca} = \dfrac{\mu v'}{\gamma} \sim 10^{-6} \ll 1$, where v' is a reference cylinder velocity. This capillary number is calculated based on the properties of water at 20 °C: viscosity $\mu = 8.9\ 10^{-4}$ [Pa s] and surface tension $\gamma = 7.2\ 10^{-2}\left[\mathrm{N\ m^{-1}}\right]$).

The geometry of our problem allows a solution in bipolar cylindrical coordinates (ξ, η, z)[48,49] (Fig. 1). This coordinate system is related to Cartesian coordinates through the following equations[49]:

$$\begin{aligned} x &= c\frac{\sinh\eta}{\lambda}, \\ y &= c\frac{\sin\xi}{\lambda}, \\ z &= z \end{aligned} \tag{2}$$

where $\lambda = \cosh\eta - \cos\xi$ and $c = a\ \sinh\eta_0$ is the characteristic length of the bipolar cylindrical coordinates [m] for a given cylinder radius a. The coordinate surfaces corresponding to η, $0 \leq \eta \leq \eta_0$ form a family of nested cylinders, while the coordinate surfaces corresponding to ξ, $0 \leq \xi < 2\pi$, are cylinders truncated along the two focal points at $(x = \pm c, y = 0)$. The plane $x = 0$ ($\eta = 0$) corresponds to a circular cylinder of infinite radius. $\eta = \eta_0$ is then the cylinder with center at $(c\coth\eta_0, 0)$ and radius $r = a$. The gap between the cylinder and the liquid-gas interface is $d_0 = a\left(\cosh\eta_0 - 1\right)$. More detailed descriptions of the properties of bipolar cylindrical coordinates can be found in Ref. 50 & 51. We assume that cylinder is significantly longer compared to its

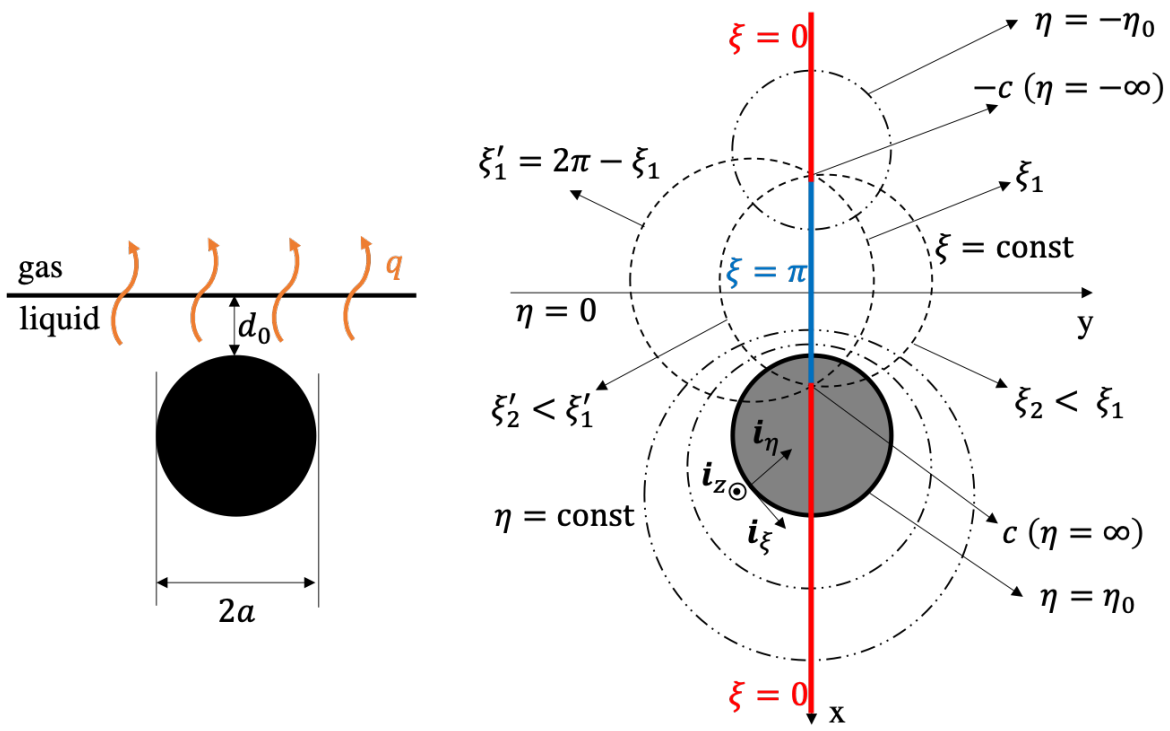

FIG. 1. On the left: schematic of a cylinder of radius a in a liquid located at a distance d_0 from a liquid-gas interface. The convective heat transfer at the liquid-gas interface is visualized by orange curved arrows. On the right: representation of the geometry in 2D bipolar cylindrical coordinates.

radius so that we can treat the problem as two-dimensional, where the axis of the infinitely long cylinder is parallel to the z-axis.

The time-dependent Navier-Stokes equation is given by[50]:

$$\rho \frac{\partial \boldsymbol{v}}{\partial t} + \rho \boldsymbol{v} \cdot \nabla \boldsymbol{v} = -\nabla p + \mu \nabla^2 \boldsymbol{v}, \tag{3}$$

where $\boldsymbol{v}$ is the liquid velocity $\left[\mathrm{m\ s^{-1}}\right]$, ρ is the density $\left[\mathrm{kg\ m^{-3}}\right]$, p is the pressure [Pa], μ is the dynamic viscosity of the liquid [Pa s], and t is time [s].

As the fluid is incompressible, and we assume that its density is constant, the fluid is divergence free:

$$\nabla \cdot \boldsymbol{v} = 0 \tag{4}$$

The velocity field obeys the following boundary conditions

$$\boldsymbol{v} = 0, \qquad x, y \to \infty \tag{5}$$

$$\boldsymbol{v} \cdot \boldsymbol{n} = 0, \qquad x = 0 \tag{6}$$

$$\boldsymbol{\tau} \cdot \boldsymbol{\sigma} \cdot \boldsymbol{n} = K_\gamma \nabla_\tau T, \qquad x = 0, \tag{7}$$

$$\boldsymbol{v} = \boldsymbol{U}_0, \qquad (x - x_0)^2 + y^2 = a^2, \quad x_0 = d_0 + a \tag{8}$$

where $\boldsymbol{n}$ is the normal to the liquid-gas interface pointing into the gas, $\boldsymbol{\tau}$ is a unit vector tangential to the liquid-gas interface, $(\boldsymbol{\tau}, \boldsymbol{n}, \boldsymbol{z} = \boldsymbol{\tau} \times \boldsymbol{n})$ form a right-handed system, ∇_τ is the gradient tangential to the liquid-gas interface, $\boldsymbol{\sigma} = \left[\nabla \boldsymbol{v} + (\nabla \boldsymbol{v})^\dagger\right] - p\mathrm{I}$ is the stress tensor, and $\boldsymbol{U}_0$ is the velocity of the cylinder in the x-direction. The fluid velocities vanish at infinity (eq. 5), and the normal component of the fluid velocity vanishes at the liquid-gas interface (eq. 6). Eq. 7 describes the tangential stress balance at the liquid-gas interface, and eq. 8 states that the cylinder moves with a velocity $\boldsymbol{U}_0$ normal to the liquid-gas interface (no-slip boundary condition). As there is no heat generation in the liquid phase and the thermal conductivity, density and thermal heat capacity of the liquid are assumed to be constant, the energy conservation equation is given by

$$\frac{\partial T}{\partial t} + \boldsymbol{v} \cdot \nabla T = \alpha \nabla^2 T, \tag{9}$$

where α is the thermal diffusivity of the liquid $\left[\mathrm{m}^2\ \mathrm{s}^{-1}\right]$. The boundary conditions for the temperature field in the liquid can be written as

$$T = T_\infty, \qquad x, y \to \infty \tag{10}$$

$$q = h\left(T - T_\infty\right), \qquad x = 0 \tag{11}$$

where q is the heat flux $\left[\mathrm{W\ m}^{-2}\right]$ on the liquid-gas interface, given by Fourier's law: $\mathbf{q} = -k\nabla T$, h is the heat convection coefficient $\left[\mathrm{W\ m}^{-2}\ \mathrm{K}^{-1}\right]$, k is the thermal conductivity of the liquid phase $\left[\mathrm{W\ m}^{-1}\ \mathrm{K}^{-1}\right]$, and T_∞ is the far field temperature in the gas and liquid [K]. Heat transfer from the liquid-gas interface into the gas phase is assumed to take place by convection, with a convection coefficient h (eq. 11). In other words, we assume that the heat reaches the liquid-gas interface by conduction and is transferred across it by convection. Our analysis considers two situations: the surface of the cylinder has a constant temperature $T = T_c$ or the heat flux on the cylinder surface is constant, $q = q_\mathrm{c}$. They represent the two limiting cases of a solid cylinder with very high ($T = T_c$) and very low thermal conductivity ($q = q_\mathrm{c}$).

The Navier-Stokes and the energy equations were made dimensionless, using the following scales[52]

$$\begin{aligned} v' &= \frac{K_\gamma \Delta T}{\mu}, & \overline{\boldsymbol{v}} &= \frac{\boldsymbol{v}}{v'} \\ t' &= \frac{a}{v'}, & \bar{t} &= \frac{t}{t'} \\ p' &= \frac{K_\gamma \Delta T}{a}, & \overline{p} &= \frac{p}{p'}, \\ \Theta &= \frac{T - T_\infty}{\Delta T}, & \overline{\boldsymbol{\sigma}} &= \left[\overline{\nabla}\overline{\boldsymbol{v}} + \left(\overline{\nabla}\overline{\boldsymbol{v}}\right)^\dagger\right] - \overline{p}\mathrm{I} \end{aligned} \tag{12}$$

where Θ is the dimensionless temperature and $\overline{\boldsymbol{\sigma}}$ is the dimensionless stress tensor. The reference velocity is derived from the Marangoni balance of surface tension forces and viscous stresses: $\mu v' \sim \gamma$. All lengths are made dimensionless by the radius of the cylinder a. ΔT is the same for both the constant temperature and the constant heat flux case as $\Delta T = T_c - T_\infty$, where T_c is the constant surface temperature in the former case and the average temperature of the cylinder in the latter case. The choice of the temperature difference $\Delta T = 0.1$ K in our calculations was motivated by the experimental and numerical analysis of the thermocapillary motion of a gear in the work of Maggi *et al.*[39]. When the total power absorbed by a micro-gear is 0.5 μW (heat flux of $q \sim 2-3$ kW m^{-2}), the estimated temperature difference per unit length driving the thermocapillary motion is $\dfrac{\Delta T}{\Delta \mathrm{L}} \sim 10$ mK μm^{-1}. By multiplying the temperature difference per unit length by the radius of the gear, we find a temperature difference ΔT of about 0.1 K.

Non-dimensionalization of eq. 3–4 and eq. 9 gives:

$$\mathrm{Re}\left[\frac{\partial \overline{\boldsymbol{v}}}{\partial \bar{t}} + \overline{\boldsymbol{v}} \cdot \overline{\nabla}\overline{\boldsymbol{v}}\right] = -\overline{\nabla}\overline{p} + \overline{\nabla}^2\overline{\boldsymbol{v}} \tag{13a}$$

$$\mathrm{Ma}\left[\frac{\partial \Theta}{\partial \bar{t}} + \overline{\boldsymbol{v}} \cdot \overline{\nabla}\Theta\right] = \overline{\nabla}^2\Theta, \tag{13b}$$

$$\overline{\nabla} \cdot \overline{\boldsymbol{v}} = 0, \tag{13c}$$

where Re and Ma are the Reynolds and Marangoni number, which are defined as:

$$\begin{aligned} \mathrm{Re} &= \frac{a v'}{\nu}, \\ \mathrm{Ma} &= \frac{a v'}{\alpha} = \frac{K_\gamma a \Delta T}{\mu \alpha} \end{aligned} \tag{14}$$

The non-dimensional boundary conditions at infinity $(x/a, y/a \to \infty)$ are given by:

$$\overline{\boldsymbol{v}} = 0, \tag{15}$$

$$\Theta = 0 \tag{16}$$

At the liquid-gas interface ($x/a = 0$), the non-dimensionalization of eq. 6–7 and eq. 11 results in:

$$\overline{\boldsymbol{v}} \cdot \boldsymbol{n} = 0, \tag{17}$$

$$\boldsymbol{\tau} \cdot \overline{\boldsymbol{\sigma}} \cdot \boldsymbol{n} = \overline{\nabla}_{\tau} \Theta \tag{18}$$

$$\frac{\partial \Theta}{\partial n} + \mathrm{Bi}\Theta = 0, \tag{19}$$

where $\mathrm{Bi} = \dfrac{ha}{k}$ is the dimensionless Biot number which is the ratio of the rate at which heat is transported by convection at the liquid-gas interface divided by the rate at which heat is transported by conduction in the liquid to the liquid-gas interface. Non-dimensional boundary conditions at the cylinder surface $\left([x/a - x_0/a]^2 + [y/a]^2 = 1,\ x_0/a = d + 1\right)$ are given by:

$$\Theta = 1, \tag{20}$$

$$\frac{\partial \Theta}{\partial n} = -\mathrm{K_q}, \tag{21}$$

$$\overline{\boldsymbol{v}} = U, \tag{22}$$

where eq. 20 and eq. 21 represents the constant temperature and the constant heat flux on the surface of the cylinder, respectively. U is the dimensionless velocity of cylinder in x-direction, $d = d_0/a$ is the dimensionless separation distance between the cylinder and the liquid-gas interface, and $\mathrm{K_q} = \dfrac{q_c a}{k\Delta T}$ is the dimensionless heat flux on the surface of the cylinder.

The Marangoni number of eq. 14 equals the Reynolds number times the Prandtl number, thus at fixed Reynolds number the magnitude of Ma is defined by the Prandtl number (appendix A, Table I), which depends only on fluid properties, and is given as:

$$\mathrm{Pr} = \frac{\nu}{\alpha} \tag{23}$$

As shown in Table I, both Reynolds and Marangoni numbers are small for micron-sized objects (assuming a radius $a = 1\ \mu$m) for a range of liquids. In the case of water, the Reynolds and Marangoni number for micron-sized particle are $\sim 10^{-3}$. As one can see in Table I, the Marangoni number is always smaller than 1, and Marangoni stresses are thus smaller than the viscous stress.

As can be seen from eqs. 13–22, the solutions for the temperature and velocity distribution depend only on five dimensionless numbers: the Biot number, the Reynolds number, the thermal Marangoni number, the dimensionless flux of the isoflux cylinder $\mathrm{K_q}$ or the dimensionless (constant) temperature Θ of the isothermal cylinder and the dimensionless gap d.

For small Reynolds and Marangoni numbers, the left hand sides of eq. 13a & 13b can be disregarded and the velocity and temperature distribution can be described by quasi-steady state equations (eq. 24 & 25). This implies that the velocity and temperature fields achieve the steady state conditions faster than is required for the cylinder to move.

$$-\overline{\nabla}\overline{p}+\overline{\nabla}^2\overline{\boldsymbol{v}}=0 \tag{24}$$

$$\overline{\nabla}^2\Theta=0 \tag{25}$$

$$\overline{\nabla}\cdot\overline{\boldsymbol{v}}=0 \tag{26}$$

As the flow is two-dimensional, we can replace eqs. 24 & 26 by:

$$E^4\Psi=0, \tag{27}$$

where Ψ is a dimensionless stream function and E^2 is the Stokes operator, which is given by[53]:

$$E^2E^2\Psi=\left(\frac{\lambda}{\overline{c}}\right)^2\left(\frac{\partial^2}{\partial\xi^2}+\frac{\partial^2}{\partial\eta^2}\right)\left[\left(\frac{\lambda}{\overline{c}}\right)^2\left(\frac{\partial^2}{\partial\xi^2}+\frac{\partial^2}{\partial\eta^2}\right)\right]\Psi, \tag{28}$$

where $\overline{c}=c/a=\sinh\eta_0$ is the dimensionless characteristic length of the bipolar cylindrical coordinates system. The velocities in bipolar cylindrical coordinates are derived from the stream function as:

$$\begin{aligned}\overline{v}_\eta&=\frac{\lambda}{\overline{c}}\frac{\partial\Psi}{\partial\xi},\\ \overline{v}_\xi&=-\frac{\lambda}{\overline{c}}\frac{\partial\Psi}{\partial\eta},\end{aligned} \tag{29}$$

With the use of eq. 29, the boundary conditions for the fluid velocities can be rewritten in terms of the stream function:

$$\Psi=0, \qquad \xi,\eta\to 0 \tag{30}$$

$$\frac{\partial\Psi}{\partial\eta}=\frac{U\overline{c}\sinh\eta\sin\xi}{\lambda^2}, \qquad \eta=\eta_0 \tag{31}$$

$$\frac{\partial\Psi}{\partial\xi}=-\frac{U\overline{c}\left(\cosh\eta\cos\xi-1\right)}{\lambda^2}, \qquad \eta=\eta_0 \tag{32}$$

$$\Psi=0, \qquad \eta=0 \tag{33}$$

$$\boldsymbol{i}_\eta\cdot\overline{\boldsymbol{\sigma}}\cdot\boldsymbol{i}_\xi=\frac{\lambda}{\overline{c}}\frac{\partial\Theta}{\partial\xi}, \qquad \eta=0, \tag{34}$$

Velocities in the fluid vanish at infinity (eq. 30), the cylinder has a no-slip surface boundary (eq. 31–32), the normal component of the velocity vanishes at the liquid-gas interface (eq. 33), and eq.

34 represents the tangential stress balance on the liquid-gas interface, which is defined in appendix E with the inverse unit vector conversions $\boldsymbol{i}$ for bipolar cylindrical coordinates.

The boundary conditions in eq. 16 and eq. 19 imposed on the energy conservation equation (eq. 25) can be rewritten by application of Fourier's law and transformation to bipolar cylindrical coordinates as:

$$\Theta = 0, \qquad \xi, \eta \to 0, \tag{35}$$

$$\frac{\lambda}{\bar{c}}\frac{\partial \Theta}{\partial \eta} + \mathrm{Bi}\Theta = 0, \qquad \eta = 0, \tag{36}$$

The boundary conditions on the surface of the cylinder for our two cases, in bipolar cylindrical coordinates, can now be written as: (i) constant temperature on the surface of the cylinder:

$$\Theta = 1, \quad \eta = \eta_0 \tag{37}$$

(ii) constant heat flux on the surface of the cylinder:

$$\frac{\lambda}{\bar{c}}\frac{\partial \Theta}{\partial \eta} = -\mathrm{K_q}, \quad \eta = \eta_0, \tag{38}$$

The constant heat flux q was chosen such that the average surface temperature for the constant flux case is the same as in the isothermal case:

$$\frac{1}{S}\int_S \Theta \mathrm{d}S = 1, \tag{39}$$

where $S = S_0/a^2$ is the dimensionless surface area of cylinder per unit length, with S_0 the surface area of the cylinder per unit length. Eq. 39 can be rewritten in bipolar coordinates as:

$$\frac{c}{\pi}\int_0^{\pi} \frac{1}{\lambda_{\eta=\eta_0}} \Theta_{\eta=\eta_0} \mathrm{d}\xi = 1, \tag{40}$$

The temperature field obeys the Laplace equation, which has a general solution obtained by separation of variables in bipolar cylindrical coordinates in the following form[54,55]:

$$\begin{aligned} \Theta = G_0 + G_1\eta + \sum_{n=1}^{\infty} \left[R_n \cosh(n\eta) + S_n \sinh(n\eta)\right]\cos(n\xi) + \\ + \sum_{n=1}^{\infty} \left[R'_n \cosh(n\eta) + S'_n \sinh(n\eta)\right]\sin(n\xi) \end{aligned} \tag{41}$$

Due to the symmetry of the system around the $y = 0$ plane, $R'_n = S'_n = 0$. The remaining coefficients R_n, S_n, G_0 and G_1 in eq. 41 were found numerically after imposing the corresponding boundary conditions. The procedure is given in appendix B.

After obtaining the temperature distribution, the solution for fluid flow can be found from eq. 27 with boundary conditions given in eq. 30–34. A general solution to equation 27 in bipolar cylindrical coordinates is given by[56,57]:

$$\Psi = \frac{\bar{c}}{\lambda}\Bigg[A\eta\lambda + (B+C\eta)\sinh\eta - D\eta\sin\xi + \\ + \sum_{n=1}^{\infty}\left[a_n\cosh(n+1)\eta + b_n\sinh(n+1)\eta + c_n\cosh(n-1)\eta + d_n\sinh(n-1)\eta\right]\cos n\xi + \\ + \sum_{n=1}^{\infty}\left[a'_n\cosh(n+1)\eta + b'_n\sinh(n+1)\eta + c'_n\cosh(n-1)\eta + d'_n\sinh(n-1)\eta\right]\sin n\xi\Bigg] \tag{42}$$

Since eq. 27 which governs the fluid velocities is a linear equation, the stream function and hence the flow field can be decomposed in two parts:

$$\Psi = \Psi_1 + \Psi_2 \tag{43}$$

The first part Ψ_1 is the creeping flow in the vicinity of the cylinder moving with a velocity U along the x-axis without interfacial tension gradients at $\eta = 0$, defined by the boundary conditions in eq. 30–33. The second part is the flow around the stationary cylinder induced by the interfacial tension gradients. Taking the boundary conditions in eq. 30–34, in which $U = 0$, into account results in the stream function Ψ_2. The derivation of an analytic solution for both Ψ_1 and Ψ_2 can be found in appendix C and the solutions are:

$$\Psi_1 = \frac{U\bar{c}}{\lambda\,(2\eta_0 - \tanh 2\eta_0)}\left(2\eta - \frac{\sinh 2\eta}{\cosh 2\eta_0}\right)\sin\xi \tag{44}$$

$$\Psi_2 = -\frac{R_1}{4\lambda}\Bigg[-\frac{2\,(1-\cosh 2\eta_0)}{\cosh 2\eta_0\,(2\eta_0 - \tanh 2\eta_0)}\eta + \cosh 2\eta \\ + \frac{(1-\cosh 2\eta_0)}{\cosh^2 2\eta_0\,(2\eta_0 - \tanh 2\eta_0)}\sinh 2\eta - \tanh 2\eta_0\sinh 2\eta - 1\Bigg]\sin\xi \tag{45}$$

The total dimensionless force exerted on the cylinder is given by[57]:

$$\boldsymbol{F} = 4\pi D\boldsymbol{i}_x \tag{46}$$

Note that this force is made dimensionless by dividing by $K_\gamma \Delta T$. There is no torque exerted on the cylinder translating perpendicular to the wall[58]. The forces exerted on the cylinder are derived from eq. C2 and C7 and are equal to:

$$\boldsymbol{F}_1 = -4\pi\frac{2U}{2\eta_0 - \tanh 2\eta_0}\boldsymbol{i}_x \tag{47}$$

$$\boldsymbol{F}_2 = 4\pi\frac{2a'_1\,(1-\cosh 2\eta_0)}{\cosh 2\eta_0\,(2\eta_0 - \tanh 2\eta_0)}\boldsymbol{i}_x \tag{48}$$

where $\boldsymbol{F}_1$ is the resistance that the cylinder experiences from the fluid in-between the cylinder and the liquid-gas interface boundary as it approaches this boundary with a velocity U, and $\boldsymbol{F}_2$ is the force the cylinder feels arising from the relative velocity of the fluid flow passed the cylinder, caused by the Marangoni stresses on the liquid-gas interface, which drags the cylinder towards the interface. The unknown velocity U of the cylinder can be found from the condition that the net force acting on the cylinder is zero[48]:

$$\boldsymbol{F}_1 + \boldsymbol{F}_2 = 0, \tag{49}$$

Using the condition in eq. 49, one can find the unknown velocity of the cylinder:

$$U = \frac{a_1' \left(1 - \cosh 2\eta_0\right)}{\cosh 2\eta_0} \tag{50}$$

The dimensionless velocity as a function of dimensionless separation distance $d = \cosh \eta_0 - 1$ between the cylinder and the liquid-gas interface in both cases is then given by:

$$U = \frac{R_1 d \left(d+2\right)}{\left[4d \left(d+2\right)+2\right] \sqrt{\left(d+1\right)^2 - 1}} \tag{51}$$

When the surface of the cylinder is warmer than the ambient temperature T_∞, the cylinder moves towards the liquid-gas interface.

III. RESULTS AND DISCUSSION

Our analysis considers free convection across a liquid-gas interface. As the thermal conductivity of a gas is much smaller than that of a liquid, the transfer of heat to the gas side is generally the limiting factor in the heat transfer. With the convection coefficient at a liquid-gas interface approximately equal to that at a solid-gas interface, for free convection, this value is $\sim 5 - 10$ W m^{-2} K^{-1}, which corresponds to a Biot number of $\sim 10^{-6} - 10^{-5}$.

The temperature distribution around the cylinder near a convective liquid-gas interface is shown in Fig. 2A. The temperature gradient at the liquid-gas interface is larger for the case of a constant heat flux on the cylinder surface (Fig. 2C), and the temperature at the interface can exceed $\Theta = 1$ in this case, while for the cylinder with constant temperature, $0 \leq \Theta \leq 1$. This larger gradient explains the larger velocity of the isoflux cylinder when compared to the isothermal cylinder. Due to the lower heat flux on the cylinder surface in case of a constant surface temperature as the cylinder approaches a liquid-gas interface, the temperature gradient increases slower than in the case of

a constant heat flux boundary condition on the cylinder surface. Therefore, the cylinder moves faster at small d in case of constant heat flux on its surface compared to a constant temperature boundary condition. For $d > 2$ the temperature gradients at the liquid-gas interface are similar in both cases, which implies that the thermocapillary velocity of the cylinder in both cases will be identical at larger distances from the liquid-gas interface.

The dimensionless cylinder velocities for both cases as a function of separation distance d are shown on Fig. 2B. At small separation distances d, the hydrodynamic drag increases without bound while the force exerted by the thermocapillary effect remains bounded. Therefore, at small d, the thermocapillary velocity goes to zero. The main limitation of the obtained results at very small separation distances is related to the lubrication forces exerted by the liquid on the cylinder. In our calculations, we consider a mathematically smooth liquid-gas interface as well as a perfectly smooth cylinder surface, which results in a lubrication singularity. In reality, such an analysis breaks down at length scales comparable to either the molecular size of water or the roughness of the cylinder. For large values of the separation distance, the thermocapillary velocity also goes to zero, since the hydrodynamic force reaches a constant value while the force exerted by the thermocapillary flow gradually decreases due to the smaller temperature gradients at the liquid-gas interface. Therefore, at an intermediate separation distance, the thermocapillary velocity reaches a maximum, located at $d \sim 0.21$ for the case of a constant heat flux and at $d \sim 0.46$ for the isothermal cylinder. A similar tendency was also obtained by Leshansky *et al.*[41] for a spherical particle with a heat source at the particle center or a constant temperature of the particle surface near an insulating liquid-gas interface. However, the velocity of a spherical particle is larger than that of a cylinder, e.g. in the case of constant heat flux the maximum dimensionless velocity of the cylinder is $U = 0.022$, whereas for the sphere it is[41] $U = 0.140$. This is due to the larger resistance to the motion of a cylinder compared to a sphere, thus to the larger hydrodynamic drag F_1 in the case of cylinder. Furthermore, the thermocapillary force F_2 is larger for a sphere as the flow pushes the particle in all directions along its axis, while for a cylinder the flow is restricted in 2D.

The largest velocity caused by a temperature difference of $\Delta T = 0.1$ K is ~ 300 μm s^{-1} in the case of constant heat flux, which is about twice as fast as the fastest reported self-electrophoretic nanoswimmer[59].

An analytical expression for the asymptotic behaviour of the velocity at large distances between a cylinder and a liquid-gas interface can be found for the case of constant heat flux on the surface of a cylinder by taking the limit $d \to \infty$ in eq. B14 and B17, and by applying the relations $d =$

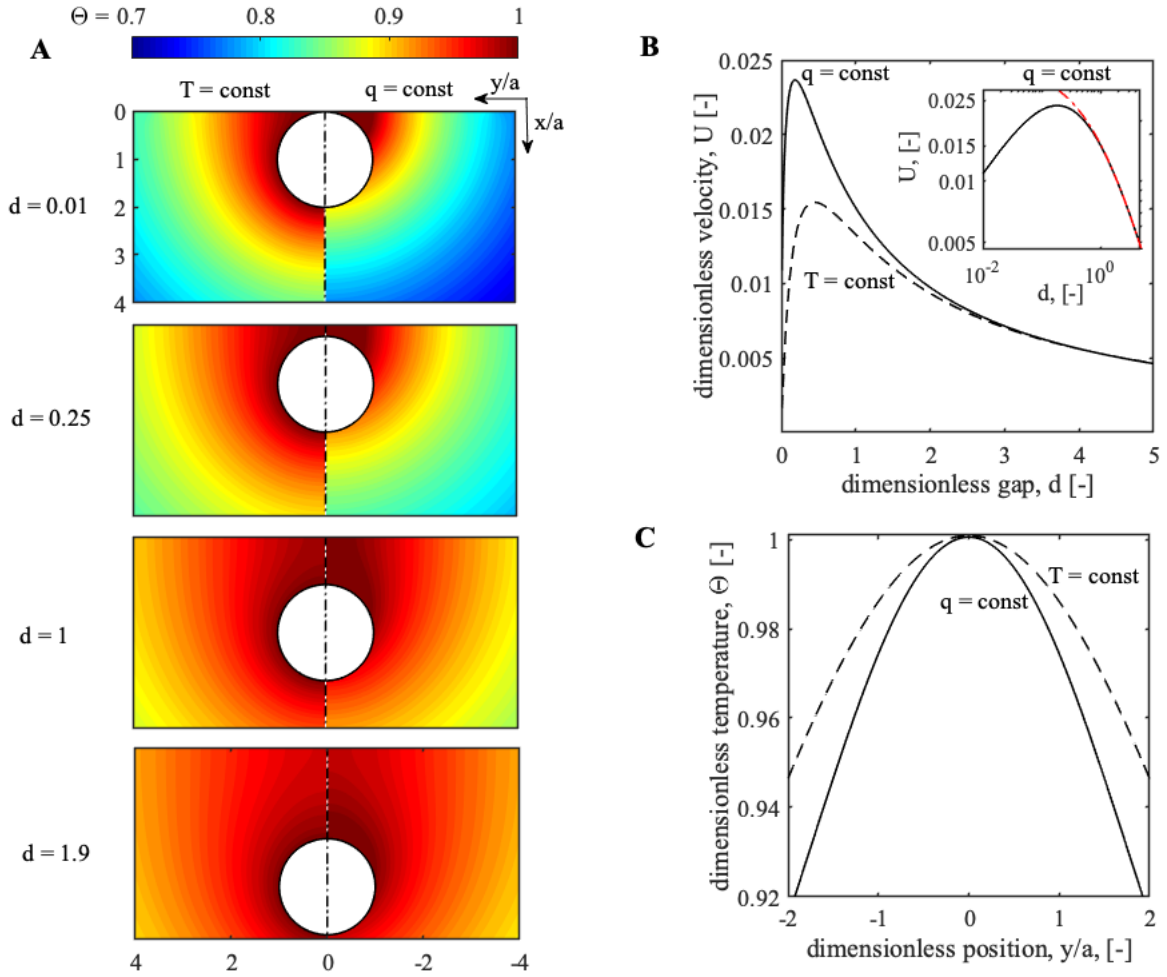

FIG. 2. A: Temperature distribution for a cylinder located near the convective liquid-gas interface for different separation distances d. The left half of the graph is is the isothermal and the right half the isoflux case. Note that the temperature scale for Θ starts at 0.7. B: Dependence of the dimensionless cylinder's velocity U on separation distance d from the convective liquid-gas interface. Solid line: constant heat flux on the surface of the cylinder; dashed line: a constant temperature on the surface of the cylinder. Inset: a constant heat flux on the surface of the cylinder; solid line: velocity dependence on the separation distance; dash-dotted line: the asymptotic dependence of the velocity on the separation distance at large distances. C: The temperature gradient at the liquid-gas interface for $d = 0.25$; dashed line: constant temperature of the cylinder's surface; solid line: constant heat flux through the surface of the cylinder. For all images: water was chosen as a model liquid, with $K_\gamma = 1.49\ 10^{-4}$ N m^{-1} K^{-1}, heat transfer coefficient for a free convection between a liquid and a gas $h = 5$ W m^{-2} K^{-1} (Bi $= 8.5 \cdot 10^{-6}$), and a dimensionless heat flux on the surface of the cylinder $K_q = 0.06$ ($\Delta T = 10^{-1}$ K, $q_c = 3.6$ kW m^{-2}).

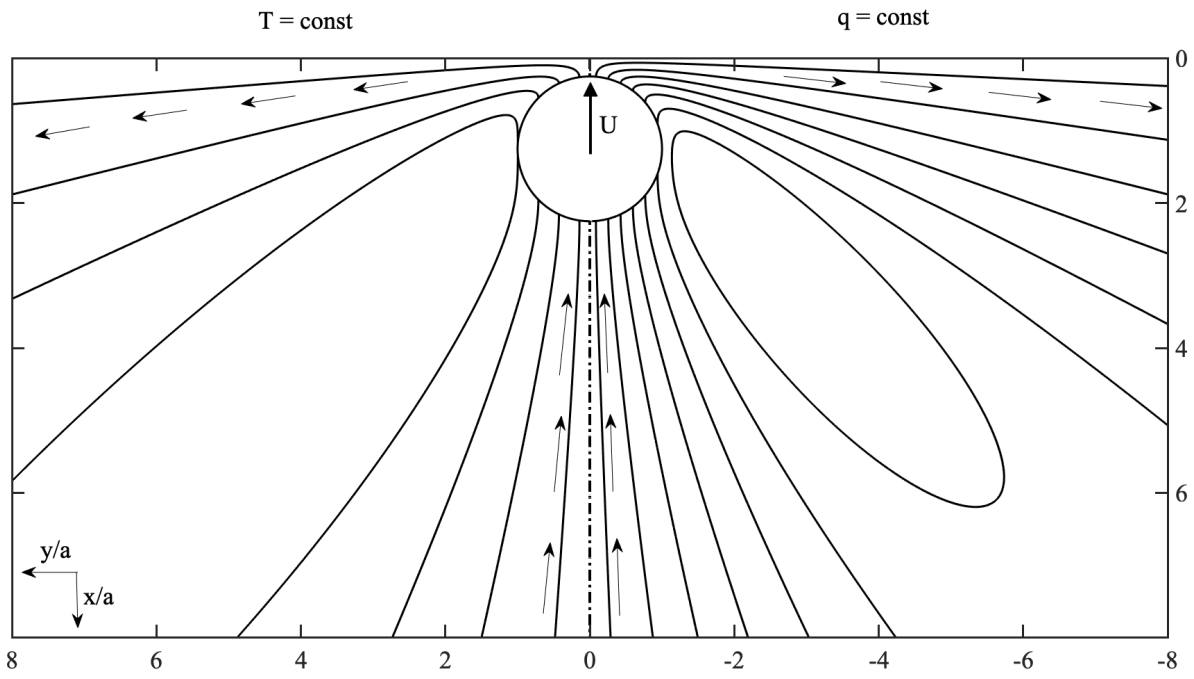

FIG. 3. Fluid streamlines around a solid cylinder moving perpendicular towards the convective liquid-gas interface by the thermocapillary effect, at a dimensionless separation distance parameter $d = 0.25$; the Biot number is $\mathrm{Bi} = 8.5 \cdot 10^{-6}$, and a dimensionless heat flux on the surface of the cylinder $K_q = 0.06$, the difference between adjacent lines is $\Delta\Psi = 0.004$. On the left: constant temperature of the cylinder's surface; on the right: constant heat flux on the surface of the cylinder. The arrows indicate the direction of the fluid flow.

$\cosh\eta_0 - 1$ and $c = a\ \sinh\eta_0$. As $\eta_0 \to \infty$, $\sinh\eta_0 \sim \cosh\eta_0$ at $d \to \infty$ and thus $c \sim d + 1$, the thermocapillary velocity scales as $U \approx -\dfrac{K_q}{2\,(d+1)}$ as $d \to \infty$, which is shown in the inset of Fig. 2B.

The fluid streamlines for the isothermal and isoflux case are shown in Fig. 3 for a separation distance $d = 0.25$. Flow patterns are qualitatively similar for both cases with two circulation regions; the liquid flows from the region with lower surface tension to the less heated regions with higher surface tension. The streamlines are located closer to each other for the case of a constant heat flux on the cylinder surface, implying that the liquid moves faster than in the constant surface temperature case. The force per unit length acting on the cylinder due to thermocapillary interaction with the liquid-gas interface evaluated using eq. 48 is on the order of $10^2 - 10^3$ pN/μm per one degree of temperature difference, which is the same order of magnitude as the torque on micro-

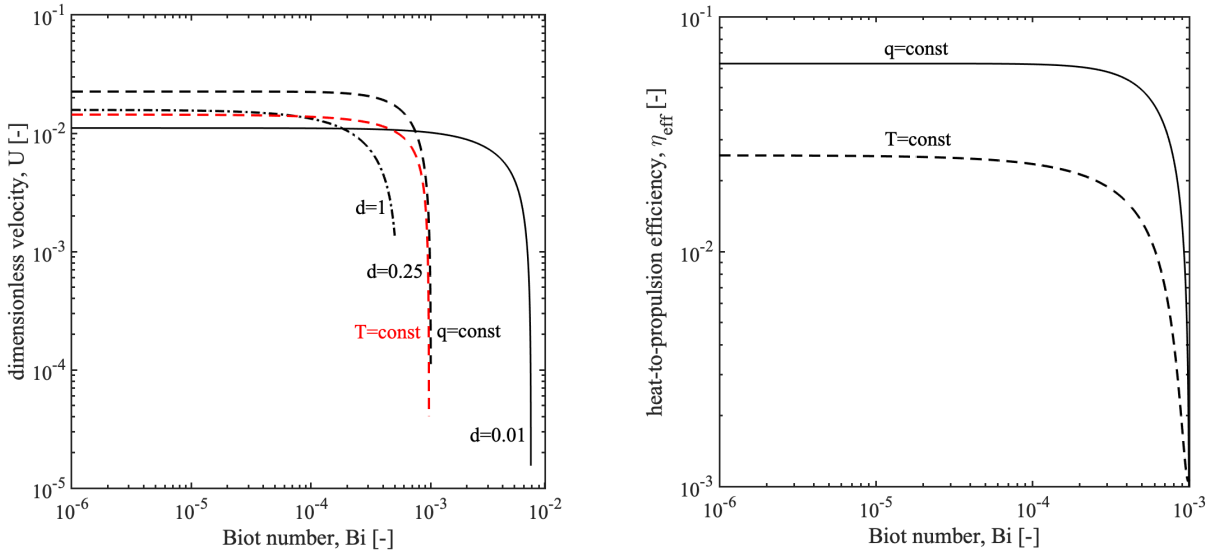

FIG. 4. On the left: dimensionless thermocapillary velocity of a cylinder as a function of the Biot number Bi at $d = 0.01$ (solid line); 0.25 (dashed line); 1 (dot-dashed line). Black lines: a constant heat flux on the cylinder surface; red line: a constant temperature on the cylinder surface. On the right: heat-to-propulsion efficiency as a function of the Biot number. Solid line: a constant heat flux; dashed line: a constant temperature on the surface of the cylinder.

gear propelled by capillary effects reported by Maggi *et al.*[39]. In accordance with calculations in [40], the thermocapillary force on a cylinder in close proximity to a liquid-gas interface is notably bigger than other reported self-phoretic forces, which are on average 0.01 – 0.5 pN/μm[44,60].

The dependence of the velocity of the cylinder on the Biot number is shown on Fig. 4. At large Biot numbers, thermal diffusion in the liquid is slow compared to convection across the liquid-gas interface, and the temperature gradients at the liquid-gas interface become small as heat is quickly removed from the interface by convection, resulting in a steep decrease of particle velocity. The onset of the drop in dimensionless velocities shifts to smaller Biot numbers when the distance between the cylinder and the liquid-gas interface increases, due to the decrease of the interfacial temperature gradient and hence surface tension gradient as the cylinder sits away further from the liquid-gas interface. This trend is similar for both the constant heat flux and the constant temperature cylinder, with smaller velocities in the latter case. At low Biot numbers, the velocity reaches a finite value corresponding to an insulating liquid-gas interface.

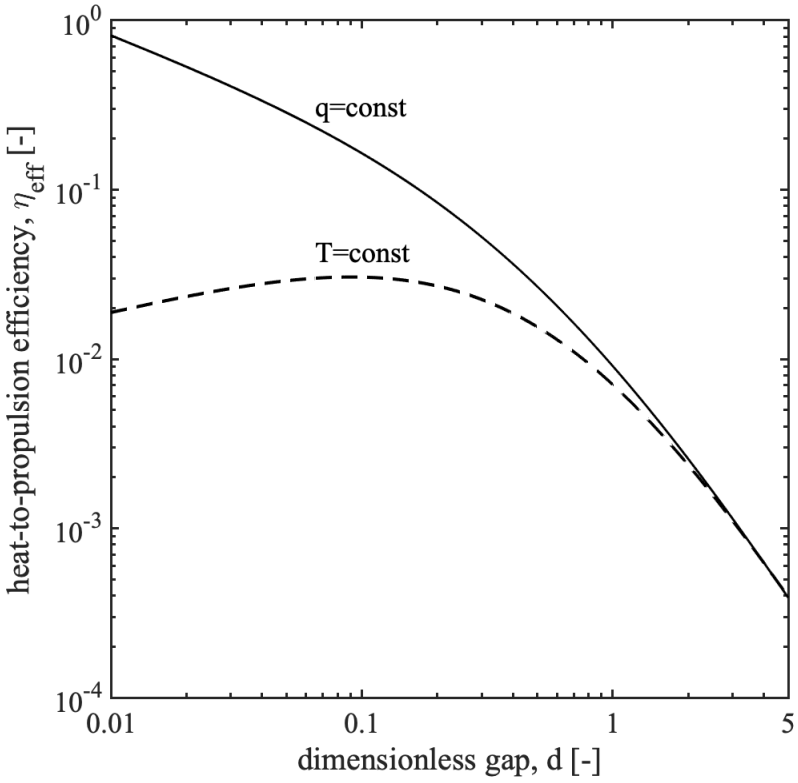

FIG. 5. Heat-to-propulsion conversion efficiency as a function of the dimensionless separation distance d from the convective liquid-gas interface for the cylinder. The solid line: a constant heat flux through the cylinder's surface; the dashed line: a constant temperature of the cylinder's surface. The constant parameters: the Biot number $\mathrm{Bi} = 8.5 \cdot 10^{-6}$, a dimensionless heat flux on the surface of the cylinder $K_q = 0.06$.

We defined a heat-to-propulsion conversion efficiency as:

$$\eta_{\mathrm{eff}} = \frac{P_{\mathrm{mech}}}{P_{\mathrm{therm}}} = \frac{F_2 U}{\mathrm{K_q} S}, \tag{52}$$

where P_{therm} is the total power input as heat, P_{mech} is the mechanical power output, the applied thermocapillary force per unit length of cylinder F_2 is defined by eq. 48, and U is defined by eq. 51. The heat-to-propulsion efficiency is on the order of $10^{-2} - 10^{-1}$, which is five orders of magnitude larger compared to the thermodynamic efficiency of the conversion of chemical energy to mechanical energy, as for example observed for $\mathrm{Pt/Au}$ Janus particles in $\mathrm{H_2O_2}$ solution[61]. This is related to the difference between thermal and mass diffusivities, which are represented by the Prandtl and Schmidt ($\mathrm{Sc} = \nu / D_{\mathrm{m}}$) numbers respectively. The Prandtl number for water is ≈ 10 at 25 °C, whereas the Schmidt number in water is usually orders of magnitude larger, for example

Sc ~ 450 for a self-electrophoresis, with protons as active species[61], as the diffusion coefficient of protons in water is about $4 \cdot 10^{-9}$ m^2 s^{-1} and the kinematic viscosity $1.8 \cdot 10^{-6}$ m^2 s^{-1}. For the thermocapillary induced motion, the thermal and momentum diffusivities are of the same order, whereas for the self-electrophoresis the momentum diffusivity dominates the mass diffusivity, which will lead to larger gradients in the former case. This also leads to the conclusion that the efficiency of Marangoni motion of a cylinder, which for example releases surface-active molecules near the liquid-gas interface, should be lower than that of thermocapillary motion, because the mass diffusivity is much smaller than the thermal diffusivity, resulting in larger Biot number and hence a lower efficiency in this case. Obviously, the thermocapillary driven cylinders are efficient only in the close proximity to the liquid-gas interface, at distances comparable to the radius of the cylinder (Fig. 5).

The heat-to-propulsion efficiency of the thermocapillary motion of the cylinder with a constant heat flux is larger than of the cylinder with a constant temperature of the surface due to the larger thermocapillary force produced by a steeper temperature gradient at the liquid-gas interface. The efficiency lowers at Bi $\sim 10^{-3}$ (Fig. 4) with the decrease of the thermocapillary force. At small separation distances d, the efficiency of a constant heat flux cylinder continuously increases with decreasing gap height (Fig. 5) because the temperature distribution at the liquid-gas interface is constantly changing as the temperature near the contact point increases without bound. However, for the constant temperature cylinder, as the temperature cannot exceed $\Theta = 1$, the efficiency experiences a slight drop at small distances, because the temperature profile for the isothermal case does not almost change as the cylinder approaches the liquid-gas interface.

IV. CONCLUSIONS

Thermocapillary motion of a solid cylinder perpendicular to a convective liquid-gas interface was studied for two different conditions at the cylinder surface: (i) for a constant temperature and (ii) for a constant heat flux. Solving the problem using bipolar cylindrical coordinates allows to find the fluid flow distribution and forces acting on the cylinder in close proximity to the liquid-gas interface. The temperature gradient at the liquid-gas interface is larger for the constant heat flux than for the constant temperature cylinder, which gives rise to the faster fluid motion around the cylinder in the former case. The dimensionless cylinder velocity U reaches a maximum at intermediate separation distances d, and is larger for the case of constant heat flux than for a constant

temperature on the cylinder surface. With an increase of the coefficient of heat transfer across the liquid-gas interface, at Biot numbers of $\sim 10^{-3}$, the velocity and the heat-to-propulsion efficiency drops. Our findings reveal that the thermocapillary mechanism results in substantial forces and can thus be exploited for the self-generated motion of micro-particles. Moreover, the efficiency of propulsion is several order of magnitudes larger for the thermocapillary motion compared to the self-phoretic mechanisms involving (electro-)chemical reactions.

ACKNOWLEDGMENTS

The authors would like to acknowledge financial support from the FWO (Research Foundation Flanders, FWO project G077916N). G.N. acknowledge funding from NSERC grant RGPIN-2017-03783. We also would like to thank Dr. Senne Fransen for the helpful discussions.

DATA AVAILABILITY STATEMENT

The data that support the findings of this study are available from the corresponding author upon reasonable request.

List of symbols

α	thermal diffusivity of the liquid	$\left[\mathrm{m^2\ s^{-1}}\right]$
γ	surface tension of the liquid-gas interface	$\left[\mathrm{N\ m^{-1}}\right]$
$\Theta = \dfrac{T - T_\infty}{\Delta T}$	dimensionless temperature	$[-]$
μ	dynamic viscosity of the liquid	[Pa s]
ν	kinematic viscosity of the liquid	$\left[\mathrm{m^2\ s^{-1}}\right]$
ξ, η	dimensionless bipolar cylindrical coordinates	$[-]$
ρ	density of the liquid	$\left[\mathrm{kg\ m^{-3}}\right]$
σ	stress	[Pa]
ψ	dimensionless stream function	$[-]$
A, B, C, D	coefficients for the stream function	$[-]$
a_n, b_n, c_n, d_n	coefficients for the stream function	$[-]$
$a_n^{'}, b_n^{'}, c_n^{'}, d_n^{'}$	coefficients for the stream function	$[-]$
a	radius of the cylinder	[m]

$\mathrm{Bi} = \dfrac{ha}{k}$	Biot number	$[-]$
c	characteristic length of the bipolar cylindrical system	$[\mathrm{m}]$
d_0	gap between the cylinder and liquid-gas interface	$[\mathrm{m}]$
$d = \dfrac{d_0}{a}$	dimensionless gap between the cylinder and liquid-gas interface	$[-]$
D_m	mass diffusivity	$\left[\mathrm{m^2\ s^{-1}}\right]$
F	dimensionless force	$[-]$
G_0, G_1, R_n, S_n	coefficients for the temperature field	$[-]$
h	heat convection coefficient between the liquid and gas phases	$\left[\mathrm{W\ m^{-2}\ K^{-1}}\right]$
k	thermal conductivity of the liquid phase	$\left[\mathrm{W\ m^{-1}\ K^{-1}}\right]$
$K_\gamma = \left\lvert \dfrac{\partial \gamma}{\partial T} \right\rvert$	coefficient of temperature dependence of surface tension	$\left[\mathrm{N\ m^{-1}\ K^{-1}}\right]$
$\mathrm{K}_q = \dfrac{q_c a}{k\Delta T}$	dimensionless heat flux	$[-]$
$\mathrm{Ma} = \dfrac{av'}{\alpha}$	Marangoni number	$[-]$
p	fluid dynamic pressure in the liquid	$[\mathrm{Pa}]$
$\mathrm{Pr} = \dfrac{\nu}{\alpha}$	Prandtl number	$[-]$
q	constant heat flux on the surface of the solid cylinder	$\left[\mathrm{W\ m^{-2}}\right]$
$\mathrm{Re} = \dfrac{av'}{\nu}$	Reynolds number	$[-]$
S_0	surface area of cylinder per unit length	$[\mathrm{m}]$
$S = \dfrac{S_0}{a^2}$	dimensionless surface area of cylinder per unit length	$[-]$
$\mathrm{Sc} = \dfrac{\nu}{D}$	Schmidt number	$[-]$
T_c	constant surface temperature of the solid cylinder	$[\mathrm{K}]$
T_∞	far-field temperature of the gas and the liquid	$[\mathrm{K}]$
U_0	velocity of the cylinder	$\left[\mathrm{m\ s^{-1}}\right]$
U	dimensionless velocity of the cylinder	$[-]$
$\boldsymbol{v}$	fluid velocity	$\left[\mathrm{m\ s^{-1}}\right]$
$\overline{v}_\eta, \overline{v}_\xi$	dimensionless fluid velocities in bipolar cylindrical coordinates	$[-]$
v', t', p'	reference velocity, time and pressure	$\left[\mathrm{m\ s^{-1}}\right], [\mathrm{s}], [\mathrm{Pa}]$
$\overline{v}$, $\overline{t}$ and $\overline{p}$	dimensionless velocity, time and pressure	$[-]$
x, y, z	Cartesian coordinates	$[\mathrm{m}]$

Appendix A: The temperature dependance of surface tension of water and the typical values of the dimensionless parameters

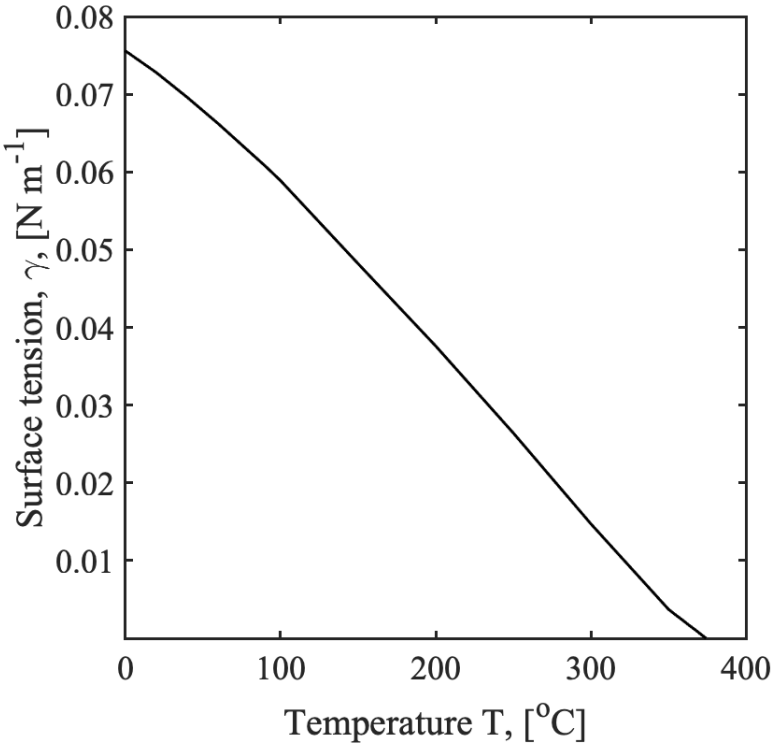

FIG. 6. The temperature dependence of surface tension of water[62]

TABLE I. Typical values of dimensionless parameters for a cylinder with a radius $a = 1\ \mu$m[63–65]

	ν [m^2 s^{-1}]	v' [m s^{-1}]	Re [–]	Pr [–]	Ma[–]
Water	10^{-6}	10^{-3}	10^{-3}	1 - 10	$10^{-3} - 10^{-2}$
Light organics	10^{-7}	10^{-3}	10^{-2}	5 - 50	$10^{-2} - 10^{-1}$
Oils	10^{-4}	10^{-4}	10^{-6}	50 - 100,000	$10^{-5} - 10^{-1}$
Liquid metals	10^{-7}	10^{-4}	10^{-3}	$4\ 10^{-3} - 3\ 10^{-2}$	$10^{-6} - 10^{-5}$

Note that v' is estimated using eq. 12 and the coefficient $K_\gamma \approx 10^{-4}$ N m^{-1} K^{-1}. The large range of Prandtl number Pr of oils is due to the wide range of their viscosities.

Appendix B: The temperature field

In this appendix we derive the coefficients for the temperature distribution around a cylindrical particle near a convective liquid-gas interface. For the case of constant temperature on the surface of the cylinder, we apply the boundary conditions of eqs. 35–37 to eq. 41:

$$G_0 + \sum_{n=1}^{\infty} R_n = 0 \tag{B1}$$

$$G_1 - G_1\cos\xi + \sum_{n=1}^{\infty} nS_n\cos(n\xi) - \sum_{n=1}^{\infty}\frac{nS_n}{2}\left(\cos\left[(n-1)\xi\right] + \cos\left[(n+1)\xi\right]\right) + \tag{B2}$$

$$+\mathrm{Bi}\bar{c}G_0 + \mathrm{Bi}\bar{c}\sum_{n=1}^{\infty} R_n\cos(n\xi) = 0$$

$$G_0 + G_1\eta_0 + \sum_{n=1}^{\infty}\left[R_n\cosh(n\eta_0) + S_n\sinh(n\eta_0)\right]\cos(n\xi) = 1 \tag{B3}$$

By multiplying eq. B2 & B3 by $\sin k\xi$ and $\cos k\xi$, $k \geq 0$, integrating between 0 and 2π, and using the orthogonality properties of the trigonometric functions, the resulting expressions become:

$$G_0 = -\sum_{n=1}^{\infty} R_n, \tag{B4}$$

$$G_1 = \frac{1 - G_0}{\eta_0}, \tag{B5}$$

$$R_n = -S_n\tanh(n\eta_0),\ n \geq 1 \tag{B6}$$

$$S_1 - 2\left(G_1 + \mathrm{Bi}\bar{c}G_0\right) = 0, \tag{B7}$$

$$-G_1 + S_1 - S_2 + \mathrm{Bi}\bar{c}R_1 = 0, \tag{B8}$$

$$2nS_n - (n+1)S_{n+1} - (n-1)S_{n-1} - 2\mathrm{Bi}\bar{c}S_n\tanh(n\eta_0) = 0,\ n \geq 2 \tag{B9}$$

Coefficients G_0, G_1, S_n, and R_n were evaluated numerically by iteration. By assuming an initial value of $G_0 = 0$, the coefficients G_1, R_n and S_n were calculated from eqs. B5–B9. Then, the initial value of G_0 was recomputed using eq. B4, followed by the re-evaluation of the coefficients. The process was repeated until eq. B4 is satisfied. A small number of coefficients is needed to find a final solution, for example, $n = 50$ gives an error below 0.3% for a dimensionless gap $d = 0.25$.

For the cylinder with a constant heat flux, the boundary conditions of eq. 35–36 & 38 are

applied to eq. 41, with the following result:

$$G_0 + \sum_{n=1}^{\infty} R_n = 0 \tag{B10}$$

$$G_1 - G_1\cos\xi + \sum_{n=1}^{\infty} nS_n\cos(n\xi) - \sum_{n=1}^{\infty}\frac{nS_n}{2}\left(\cos\left[(n-1)\xi\right] + \cos\left[(n+1)\xi\right]\right) + \tag{B11}$$
$$+\mathrm{Bi}\bar{c}G_0 + \mathrm{Bi}\bar{c}\sum_{n=1}^{\infty} R_n\cos(n\xi) = 0$$

$$\frac{1}{2}\sum_{n=1}^{\infty}\left(nR_n\sinh n\eta_0 + nS_n\cosh n\eta_0\right)\left(\cos(n+1)\xi + \cos(n-1)\xi\right) + G_1\cos\xi - \tag{B12}$$
$$-G_1\cosh\eta_0 - \cosh\eta_0\sum_{n=1}^{\infty}\left(nR_n\sinh n\eta_0 + nS_n\cosh n\eta_0\right)\cos n\xi = \mathrm{K_q}\bar{c}$$

Then, by exploiting the orthogonality properties of trigonometric functions, the resulting expressions become:

$$G_0 + \sum_{n=1}^{\infty} R_n = 0, \tag{B13}$$

$$S_1 - 2\left(G_1 + \mathrm{Bi}\bar{c}G_0\right) = 0 \tag{B14}$$

$$-G_1 + S_1 - S_2 + \mathrm{Bi}\bar{c}R_1 = 0 \tag{B15}$$

$$2nS_n - (n+1)S_{n+1} - (n-1)S_{n-1} + 2\mathrm{Bi}\bar{c}R_n = 0, \quad n \geqslant 2 \tag{B16}$$

$$-G_1\cosh\eta_0 + \frac{1}{2}\left(R_1\sinh\eta_0 + S_1\cosh\eta_0\right) = \mathrm{K_q}\bar{c}, \tag{B17}$$

$$G_1 + R_2\sinh 2\eta_0 + S_2\cosh 2\eta_0 - \frac{1}{2}R_1\sinh 2\eta_0 - S_1\cosh^2\eta_0 = 0 \tag{B18}$$

$$F_{n+1} + F_{n-1} - 2\cosh\eta_0 F_n = 0, \quad n \geqslant 2 \tag{B19}$$

$$nR_n\sinh n\eta_0 + nS_n\cosh n\eta_0 = F_n \tag{B20}$$

After solving the recurrence relation in eq. B19 with the initial conditions in eq. B17-B18 and applying eq. B20, we obtain the following recurrence relation for the coefficients R_n:

$$R_n = \frac{2G_1}{n}\coth n\eta_0 + \frac{2\mathrm{K_q}\bar{c}}{n\sinh\eta_0} - S_n\coth n\eta_0 \tag{B21}$$

Combining eq. B13 and eq. B21 and applying $\bar{c} = \sinh\eta_0$ gives:

$$G_0 = \sum_{n=1}^{\infty}\left(\frac{2G_1}{n}\coth n\eta_0 + \frac{2\mathrm{K_q}}{n} - S_n\coth n\eta_0\right) \tag{B22}$$

As at $n \to \infty$, $\coth n\eta_0 \to 1$ and $\sum_{n=1}^{\infty}\frac{1}{n}$ is divergent, for the solution to be bounded require $G_1 = -\mathrm{K_q}$. Coefficients G_0, G_1, S_n, and R_n were evaluated numerically by iteration in the same way

as in the constant temperature case. The values of first ten coefficients at $d = 0.25$ are shown in Table II. In order to obtain an error below 2% for a dimensionless gap $d = 0.25$, the number of calculated coefficients must be $n = 1000$. However, for large separation distances the number of coefficients necessary to obtain the same accuracy is much smaller. For example, at $d = 2$ only 5 coefficients are needed to have an error smaller than 1%.

TABLE II. Values of the first ten coefficients G_0, G_1, R_n, S_n for temperature field around isothermal and isoflux cylinders at separation distance $d = 0.25$, the Biot number $\mathrm{Bi} = 8.5 \cdot 10^{-6}$, a dimensionless heat flux on the surface of the cylinder $K_q = 0.06$

n	$T = \text{const}$ ($G_0 = 0.953, G_1 = 0.068$)		$q = \text{const}$ ($G_0 = 0.992, G_1 = 0.066$)	
	R_n	S_n	R_n	S_n
1	-0.081	0.135	-0.132	0.132
2	-0.060	0.068	-0.066	0.066
3	-0.044	0.045	-0.044	0.044
4	-0.034	0.034	-0.033	0.033
5	-0.027	0.027	-0.026	0.026
6	-0.023	0.023	-0.022	0.022
7	-0.019	0.019	-0.019	0.019
8	-0.017	0.017	-0.017	0.017
9	-0.015	0.015	-0.015	0.015
10	-0.014	0.014	-0.013	0.013

The coefficients show geometric convergence for both the constant temperature and the constant heat flux on the cylinder surface cases, so if $\log|R_n| = \log|C| + p\log n$, where p is the order of convergence and C is a number independent of n, then $p = -1$.

The rate of conversion is

$$\lim_{n\to\infty} R_{n+1}/R_n \approx 0.99,$$

thus it is sublinear both in the case of constant temperature and of constant heat flux cylinder.

Appendix C: The coefficients for the stream function Ψ

The coefficients in eq. 42 for the first part Ψ_1 are the same for both the cylinder with a constant temperature of the surface or with a constant heat flux and have the following values:

$$A = B = C = 0, \tag{C1}$$

$$D = -\frac{2U}{2\eta_0 - \tanh 2\eta_0}, \tag{C2}$$

$$a_1 = b_1 = c_1 = a_1' = c_1' = 0, \tag{C3}$$

$$b_1' = \frac{D}{2\cosh 2\eta_0}, \tag{C4}$$

$$a_n = b_n = c_n = d_n = a_n' = b_n' = c_n' = d_n' = 0, \quad n \geq 2 \tag{C5}$$

They are obtained by applying the boundary conditions of eq. 30–33 to eq. 42 and exploiting the orthogonality of trigonometric functions to obtain a linear system of equations for the coefficients. Similar procedure is used to obtain the parameters for the second part of the stream function Ψ_2, where the boundary conditions in eq. 30–34 with $U = 0$ are applied to eq. 42:

$$A = B = C = 0, \tag{C6}$$

$$D = \frac{2a_1'\,(1 - \cosh 2\eta_0)}{\cosh 2\eta_0\,(2\eta_0 - \tanh 2\eta_0)}, \tag{C7}$$

$$a_1 = b_1 = c_1 = 0, \tag{C8}$$

$$a_1' = \frac{R_1}{4\bar{c}}, \tag{C9}$$

$$c_1' = -a_1' \tag{C10}$$

$$b_1' = \frac{D - 2a_1' \sinh 2\eta_0}{2\cosh 2\eta_0} \tag{C11}$$

$$a_n = b_n = c_n = d_n = a_n' = b_n' = c_n' = d_n' = 0, \quad n \geq 2 \tag{C12}$$

where R_1 is the first coefficient of the temperature distribution function of appendix B, which is different for the case of constant temperature and constant heat flux. A more detailed general procedure of deriving the coefficients for a stream function can be found in the analysis of Wakiya *et al.*[57].

Appendix D: Solution for the motion of a no-slip cylinder perpendicular to a free liquid-gas interface

The solution for the two-dimensional flow around a no-slip cylinder that moves perpendicular to a free liquid-gas interface was derived in appendix C from eq. 42 with the boundary conditions in eqs. 30–33:

$$\Psi = \frac{U\overline{c}}{\lambda\left(2\eta_0 - \tanh 2\eta_0\right)}\left(2\eta - \frac{\sinh 2\eta}{\cosh 2\eta_0}\right)\sin\xi \tag{D1}$$

The dimensionless drag force on the cylinder moving perpendicular to a free liquid-gas interface was obtained from eq. 46 and coefficient D of appendix C and is shown in Fig. 7:

$$\boldsymbol{F}_d = -\frac{8\pi U}{\eta_0 - \tanh 2\eta_0}\boldsymbol{i}_x = -4\pi U\left\{\ln\left[d+1+\sqrt{(d+1)^2-1}\right] - \frac{(d+1)\sqrt{(d+1)^2-1}}{2(d+1)^2-1}\right\}^{-1}\boldsymbol{i}_x, \tag{D2}$$

When the cylinder is far away from the liquid-gas interface ($d \to \infty$), η_0 goes to infinity and the drag force in eq. D2 becomes zero. This is known as Stokes' paradox, which can be resolved by including the inertial terms in the Navier-Stokes equation, or by using the Oseen approximation. The drag per unit length of circular cylinder in an unbounded fluid was obtained by Lamb[66]:

$$\boldsymbol{F} = \frac{4\pi U}{0.5 - \gamma - \log\left(\mathrm{Re}/8\right)}, \tag{D3}$$

where $\gamma = 0.5772...$ is Eulers constant.

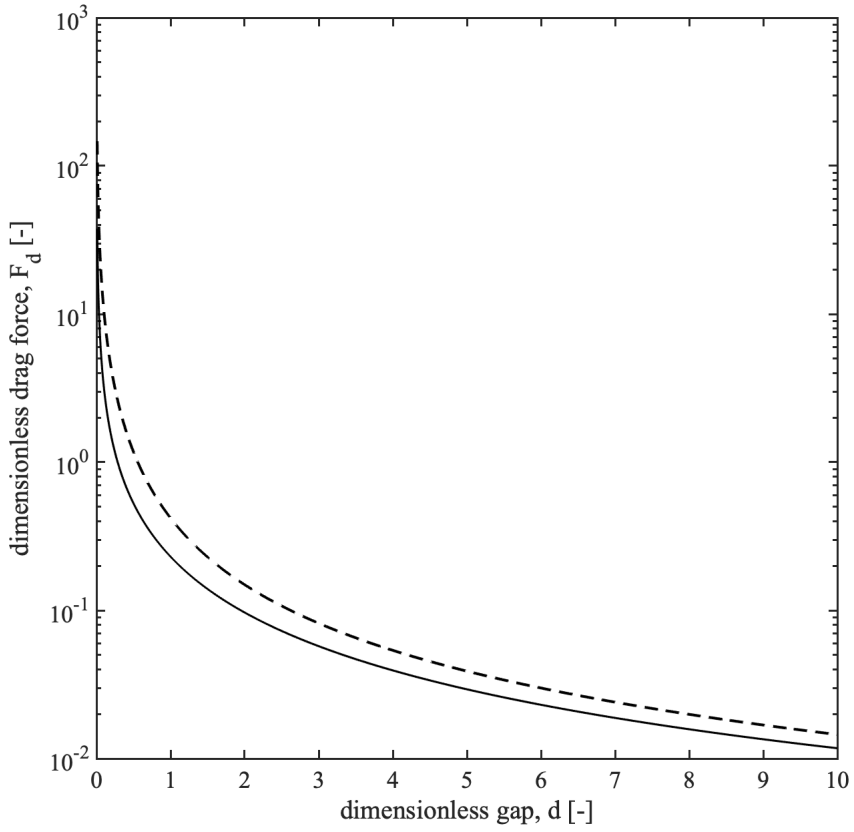

FIG. 7. Dimensionless drag force on a no-slip cylinder moving perpendicular to a free liquid-gas interface (solid line), and perpendicular to a no-slip wall[58] (dashed line) as a function of the dimensionless gap d

As can be seen in Fig. 7, at all values of the dimensionless separation distance d the force on a no-slip cylinder moving perpendicular to a free liquid-gas interface is smaller than that of a cylinder moving perpendicular to a no-slip wall, which is given by[58]:

$$F_{d,\text{wall}} = -\frac{4\pi U}{\eta_0 - \tanh\eta_0} = -4\pi U \left\{ \ln\left[d+1+\sqrt{(d+1)^2-1} \right] - \frac{\sqrt{d\,(d+2)}}{d+1} \right\}^{-1} \tag{D4}$$

Appendix E: Relations in bipolar cylindrical coordinates

$$c = \sqrt{\left(\frac{d_0}{a}+1\right)^2 - 1}, \tag{E1}$$

$$\eta_0 = \operatorname{acosh}\left(\frac{d_0}{a}+1\right) \tag{E2}$$

or

$$\eta_0 = \ln\left[\frac{d_0}{a} + 1 + \sqrt{\left(\frac{d_0}{a}+1\right)^2 - 1}\right] \tag{E3}$$

This implies that $\eta_0 \to 0$ as $\sqrt{\frac{2d_0}{a}}$ when $d_0 \to 0$.
The unit vectors conversion from bipolar cylindrical to Cartesian coordinates are given by:

$$\boldsymbol{i}_x = -\frac{1}{\lambda}\left[\sinh\eta\sin\xi\,\boldsymbol{i}_\xi + (\cosh\eta\cos\xi - 1)\,\boldsymbol{i}_\eta\right] \tag{E4}$$

$$\boldsymbol{i}_y = \frac{1}{\lambda}\left[(\cosh\eta\cos\xi - 1)\,\boldsymbol{i}_\xi - \sinh\eta\sin\xi\,\boldsymbol{i}_\eta\right] \tag{E5}$$

The inverse unit vectors conversion is given by:

$$\boldsymbol{i}_\eta = -\frac{1}{\lambda}\left[(\cosh\eta\cos\xi - 1)\,\boldsymbol{i}_x + \sinh\eta\sin\xi\,\boldsymbol{i}_y\right] \tag{E6}$$

$$\boldsymbol{i}_\xi = -\frac{1}{\lambda}\left[\sinh\eta\sin\xi\,\boldsymbol{i}_x - (\cosh\eta\cos\xi - 1)\,\boldsymbol{i}_y\right] \tag{E7}$$

The inverse transformation of bipolar cylindrical coordinates is given by:

$$\eta = \frac{1}{2}\,\log\left[\frac{(x+c)^2+y^2}{(x-c)^2+y^2}\right] \tag{E8}$$

$$\xi = \pi - 2\mathrm{atan}\left[\frac{2cy}{c^2-x^2-y^2+\sqrt{(c^2-x^2-y^2)^2+4c^2y^2}}\right] \tag{E9}$$

$$z = z \tag{E10}$$

The tangential stress boundary condition (eq. 34) was rewritten in bipolar coordinates using the dyadic product in curvilinear coordinates from Appendix A.7 in Happel and Brenner[50]

$$\boldsymbol{i}_\eta\cdot\overline{\boldsymbol{\sigma}}\cdot\boldsymbol{i}_\xi = \boldsymbol{i}_\eta\left(\left[\overline{\nabla}\overline{\boldsymbol{v}} + \left(\overline{\nabla}\overline{\boldsymbol{v}}\right)^\dagger\right] - \overline{p}\boldsymbol{I}\right)\cdot\boldsymbol{i}_\xi = \frac{1}{h_\mathrm{m}}\left(\frac{\partial v_\xi}{\partial\eta} + \frac{\partial v_\eta}{\partial\xi}\right), \tag{E11}$$

where $h_\mathrm{m} = h_\xi = h_\eta = \dfrac{\overline{c}}{\lambda}$ are the metric coefficients of the bipolar cylindrical coordinates.

REFERENCES

[1]S. Ebbens and J. Howse, "In pursuit of propulsion at the nanoscale," Soft Matter **6**, 726–738 (2010).

[2]K. Dey, F. Wong, A. Altemose, and A. Sen, "Catalytic motors—quo vadimus?" Current Opinion in Colloid and Interface Science **21**, 4–13 (2016).

[3]S. Segupta, M. Ibele, and A. Sen, "Fantastic voyage: designing self-powered nanorobots," Angew. Chem. Int. Ed. **51**, 8434–8445 (2012).

[4]D. Kagan, P. Calvo-Marzal, S. Balasubramanian, S. Sattayasamitsathit, K. Manesh, G.-U. Flechsig, and J. Wang, "Chemical sensing based on catalytic nanomotors: Motion-based detection of trace silver," J. Am. Chem. Soc. **131**, 12082–12083 (2009).

[5]S. Sundararajan, P. Lammert, A. Zudans, V. Crespi, and A. Sen, "Catalytic motors for transport of colloidal cargo," Nano Lett. **8**, 1271–1276 (2008).

[6]A. M. Boymelgreen, T. Balli, T. Miloh, and G. Yossifon, "Active colloids as mobile microelectrodes for unified label-free selective cargo transport," Nature Communications **9**, 1–8 (2018).

[7]L. Baraban, M. Tasinkevych, M. Popescu, S. Sanchez, S. Dietrich, and O. Schmidt, "Transport of cargo by catalytic Janus micro-motors," Soft Matter **8**, 48–52 (2012).

[8]W. Gao, D. Kagan, O. S. Pak, C. Clawson, S. Campuzano, E. Chuluun-Erdene, E. Shipton, E. E. Fullerton, L. Zhang, E. Lauga, and J. Wang, "Cargo-towing fuel-free magnetic nanoswimmers for targeted drug delivery," Small **8**, 460–467 (2012).

[9]J. Wang and W. Gao, "Nano/microscale motors: biomedical opportunities and challenges," ACS Nano **6**, 5745–5751 (2012).

[10]R. Ismagilov, A. Schwartz, N. Bowden, and G. Whitesides, "Autonomous movement and self-assembly," Angew. Chem. Int. Ed. **41**, 652–654 (2002).

[11]W. Paxton, K. Kistler, C. Olmeda, A. Sen, S. S. Angelo, Y. Cao, T. Mallouk, P. Lammert, and V. Crespi, "Catalytic nanomotors : Autonomous movement of striped nanorods," J. Am. Chem. Soc. **126**, 13424–13431 (2004).

[12]J. Howse, R. Jones, and A. Ryan, "Self-motile colloidal particles: from direct propulsion to random walk," Physical Review Letters **99**, 048102 (2007).

[13]J. Moran, P. Wheat, and J. Posner, "Locomotion of electrocatalytic nanomotors due to reaction induced charge autoelectrophoresis," Physical Review E **81**, 065302 (2010).

[14]W. F. Paxton, A. Sen, and T. E. Mallouk, "Motility of catalytic nanoparticles through self-generated forces," Chemistry–A European Journal **11**, 6462–6470 (2005).

[15]Y. Wang, R. M. Hernandez, D. J. Bartlett, J. M. Bingham, T. R. Kline, A. Sen, and T. E. Mallouk, "Bipolar electrochemical mechanism for the propulsion of catalytic nanomotors in hydrogen peroxide solutions," Langmuir **22**, 10451–10456 (2006).

[16]R. Golestanian, T. Liverpool, and A. Ajdari, "Designing phoretic micro-and nano-swimmers," New Journal of Physics **9**, 126 (2007).

[17]M. N. Popescu, W. E. Uspal, and S. Dietrich, "Self-diffusiophoresis of chemically active colloids," The European Physical Journal Special Topics **225**, 2189–2206 (2016).

[18]P. Malgaretti, M. Popescu, and S. Dietrich, "Self-diffusiophoresis induced by fluid interfaces," Soft Matter **14**, 1375–1388 (2018).

[19]J. G. Gibbs and Y.-P. Zhao, "Autonomously motile catalytic nanomotors by bubble propulsion," Applied Physics Letters **94**, 163104 (2009).

[20]A. A. Solovev, Y. Mei, E. Bermúdez Ureña, G. Huang, and O. G. Schmidt, "Catalytic microtubular jet engines self-propelled by accumulated gas bubbles," Small **5**, 1688–1692 (2009).

[21]K. E. Peyer, S. Tottori, F. Qiu, L. Zhang, and B. J. Nelson, "Magnetic helical micromachines," Chemistry–A European Journal **19**, 28–38 (2013).

[22]W. Wang, W. Duan, Z. Zhang, M. Sun, A. Sen, and T. E. Mallouk, "A tale of two forces: simultaneous chemical and acoustic propulsion of bimetallic micromotors," Chemical Communications **51**, 1020–1023 (2015).

[23]H.-R. Jiang, N. Yoshinaga, and M. Sano, "Active motion of a Janus particle by self-thermophoresis in a defocused laser beam," Physical Review Letters **105**, 268302 (2010).

[24]M. Yang and M. Ripoll, "Simulations of thermophoretic nanoswimmers," Physical Review E **84**, 061401 (2011).

[25]G. Volpe, I. Buttinoni, D. Vogt, H.-J. Kümmerer, and C. Bechinger, "Microswimmers in patterned environments," Soft Matter **7**, 8810–8815 (2011).

[26]I. Buttinoni, G. Volpe, F. Kümmel, G. Volpe, and C. Bechinger, "Active Brownian motion tunable by light," Journal of Physics: Condensed Matter **24**, 284129 (2012).

[27]J. R. Gomez-Solano, A. Blokhuis, and C. Bechinger, "Dynamics of self-propelled Janus particles in viscoelastic fluids," Physical Review Letters **116**, 138301 (2016).

[28]J. W. Bush and D. L. Hu, "Walking on water: biolocomotion at the interface," Annu. Rev. Fluid Mech. **38**, 339–369 (2006).

[29]R. S. Subramanian, R. Balasubramaniam, and N. Clark, "Motion of bubbles and drops in reduced gravity," Appl. Mech. Rev. **55**, B56–B57 (2002).

[30]C. C. Maass, C. Krüger, S. Herminghaus, and C. Bahr, "Swimming droplets," Annual Review of Condensed Matter Physics **7**, 171–193 (2016).

[31]S. Michelin, E. Lauga, and D. Bartolo, "Spontaneous autophoretic motion of isotropic particles,"

Physics of Fluids **25**, 061701 (2013).

[32]Z. Izri, M. N. Van Der Linden, S. Michelin, and O. Dauchot, "Self-propulsion of pure water droplets by spontaneous Marangoni-stress-driven motion," Physical Review Letters **113**, 248302 (2014).

[33]S. Nakata, Y. Iguchi, S. Ose, M. Kuboyama, T. Ishii, and K. Yoshikawa, "Self-rotation of a camphor scraping on water: new insight into the old problem," Langmuir **13**, 4454–4458 (1997).

[34]S. Nakata, M. I. Kohira, and Y. Hayashima, "Mode selection of a camphor boat in a dual-circle canal," Chemical Physics Letters **322**, 419–423 (2000).

[35]E. Bormashenko, Y. Bormashenko, R. Grynyov, H. Aharoni, G. Whyman, and B. P. Binks, "Self-propulsion of liquid marbles: Leidenfrost-like levitation driven by Marangoni flow," The Journal of Physical Chemistry C **119**, 9910–9915 (2015).

[36]E. Lauga and A. M. Davis, "Viscous Marangoni propulsion," Journal of Fluid Mechanics **705**, 120–133 (2012).

[37]A. Würger, "Thermally driven Marangoni surfers," Journal of Fluid Mechanics **752**, 589–601 (2014).

[38]H. Masoud and H. A. Stone, "A reciprocal theorem for Marangoni propulsion," Journal of Fluid Mechanics **741**, R41–R47 (2014).

[39]C. Maggi, F. Saglimbeni, M. Dipalo, F. D. Angelis, and R. D. Leonardo, "Micromotors with asymmetric shape that efficiently convert light into work by thermocapillary effects," Nature Communications **6**, 7855 (2015).

[40]A. Domínguez, P. Malgaretti, M. N. Popescu, and S. Dietrich, "Effective interaction between active colloids and fluid interfaces induced by Marangoni flows," Physical Review Letters **116**, 078301 (2016).

[41]A. Leshansky, A. Golovin, and A. Nir, "Thermocapillary interaction between a solid particle and a liquid-gas interface," Phys. Fluids **9**, 2818–2827 (1997).

[42]A. Domínguez, P. Malgaretti, M. Popescu, and S. Dietrich, "Erratum: Effective interaction between active colloids and fluid interfaces induced by Marangoni flows [phys. rev. lett. 116, 078301 (2016)]," Physical Review Letters **117** (2016).

[43]N. Reddy, L. Palangetic, L. Stappers, J. Buitenhuis, J. Fransaer, and C. Clasen, "Metallic and bimetallic Janus nanofibers: electrical and self-propulsion properties," J. Mater. Chem. **1**, 3646–3650 (2013).

[44]V. R. Dugyala, N. Reddy, J. Fransaer, and C. Clasen, "Self-propulsion of bent bimetallic Janus

rods," Journal of Physics D: Applied Physics **52**, 014002 (2018).

[45]H. R. Vutukuri, Z. Preisler, T. H. Besseling, A. Van Blaaderen, M. Dijkstra, and W. T. Huck, "Dynamic self-organization of side-propelling colloidal rods: experiments and simulations," Soft Matter **12**, 9657–9665 (2016).

[46]J. Berg, *An introduction to interfaces and colloids: the bridge to nanoscience* (World Scientific, 2010).

[47]R. Cini, G. Loglio, and A. Ficalbi, "Temperature dependence of the surface tension of water by the equilibrium ring method," Journal of Colloid and Interface Science **41**, 287–297 (1972).

[48]H. Keh, K.D.Horng, and J. Kuo, "Boundary effects on electrophoresis of colloidal cylinders," J. Fluid Mech. **231**, 211–228 (1991).

[49]P. Moon and D. Spencer, *Field Theory Handbook* (Springer-Verlag, Berlin, Heidelberg, 1988).

[50]J. Happel and H. Brenner, *Low Reynolds number hydrodynamics*, edited by S. Whitaker (Noordhoff International Publishing, 1973).

[51]P. Lucht, "Bipolar coordinates and the two-cylinder capacitor," Rimrock Digital Technology, Salt Lake City, Utah **84103** (2015).

[52]A. Rybicki and J. Floryan, "Thermocapillary effects in liquid bridges. I. Thermocapillary convection," The Physics of Fluids **30**, 1956–1972 (1987).

[53]R. Panton, *Incompressible flow* (John Wiley & Sons, 1984).

[54]A. Umemura, "Matched-asymptotic analysis of low-Reynolds-number flow past two equal circular cylinders," J. Fluid Mech. **121**, 345–363 (1982).

[55]L. Wang and H. Keh, "Electrophoretic motion of a colloidal cylinder near a plane wall," Microfluid Nanofluid **10**, 81–95 (2011).

[56]G. B. Jeffery, "The rotation of two circular cylinders in a viscous fluid," Proceedings of the Royal Society of London. Series A, Containing Papers of a Mathematical and Physical Character **101**, 169–174 (1922).

[57]S. Wakiya, "Application of bipolar coordinates to the two-dimensional creeping motion of a liquid. II. Some problems for two circular cylinders in viscous fluid," Journal of the Physical Society of Japan **39**, 1603–1607 (1975).

[58]D. Jeffrey and Y. Onishi, "The slow motion of a cylinder next to a plane wall," The Quarterly Journal of Mechanics and Applied Mathematics **34**, 129–137 (1981).

[59]U. K. Demirok, R. Laocharoensuk, K. M. Manesh, and J. Wang, "Ultrafast catalytic alloy nanomotors," Angewandte Chemie **120**, 9489–9491 (2008).

[60]J. Burdick, R. Laocharoensuk, P. M. Wheat, J. Posner, and J. Wang, "Synthetic nanomotors in microchannel networks: Directional microchip motion and controlled manipulation of cargo," Journal of the American Chemical Society **130**, 8164–8165 (2008).

[61]W. Wang, T. Chiang, D. Velegol, and T. Mallouk, "Understanding the efficiency of autonomous nano-and microscale motors," Journal of the American Chemical Society **135**, 10557–10565 (2013).

[62]N. Vargaftik, B. Volkov, and L. Voljak, "International tables of the surface tension of water," Journal of Physical and Chemical Reference Data **12**, 817–820 (1983).

[63]J. Coulson and J. Richardson, *Chemical engineering: fluid flow, heat transfer and mass transfer.* (Butterworth-Heinemann, 1999).

[64]R. Serway, *Physics for Scientists and Engineers* (Saunders College Publishing, 1996).

[65]W. M. Haynes, *CRC handbook of chemistry and physics* (CRC press, 2014).

[66]H. Lamb, "XV. On the uniform motion of a sphere through a viscous fluid," The London, Edinburgh, and Dublin Philosophical Magazine and Journal of Science **21**, 112–121 (1911).